

1 **Machine-learning reveals climate forcing from aerosols is dominated by**
2 **increased cloud cover**

3 **Ying Chen^{1*#}, Jim Haywood^{1,2}, Yu Wang³, Florent Malavelle⁴, George Jordan², Daniel**
4 **Partridge¹, Jonathan Fieldsend¹, Johannes De Leeuw⁵, Anja Schmidt^{5,6,†}, Nayeong Cho⁷,**
5 **Lazaros Oreopoulos⁷, Steven Platnick⁷, Daniel Grosvenor⁸, Paul Field^{4,9}, Ulrike**
6 **Lohmann³**

7 ¹College of Engineering, Mathematics, and Physical Sciences, University of Exeter, UK

8 ²Met Office Hadley Centre, Exeter, UK

9 ³Institute for Atmospheric and Climate Science, ETH Zurich, Zurich, Switzerland

10 ⁴Met Office, Exeter, UK

11 ⁵Centre for Atmospheric Science, Yusuf Hamied Department of Chemistry, University of
12 Cambridge, UK

13 ⁶Department of Geography, University of Cambridge, UK

14 ⁷Earth Sciences Division, NASA GSFC, Greenbelt, Maryland, USA

15 ⁸National Centre for Atmospheric Sciences, University of Leeds, Leeds, UK

16 ⁹School of Earth and Environment, University of Leeds, Leeds, UK

17 *Correspondence to: Ying Chen (y.chen6@exeter.ac.uk; ying.chen@psi.ch)

18 #Now at Laboratory of Atmospheric Chemistry, Paul Scherrer Institut, Villigen, Switzerland

19 †Now at Institute of Atmospheric Physics (IPA), German Aerospace Center (DLR),
20 Oberpfaffenhofen, Germany and Meteorological Institute, Ludwig Maximilian University of
21 Munich, Munich, Germany

22

23

24 **Abstract:**

25 **Aerosol-cloud interactions have a potentially large impact on climate, but are poorly**
26 **quantified and thus contribute a significant and long-standing uncertainty in climate**
27 **projections. The impacts derived from climate models are poorly constrained by**
28 **observations, because retrieving robust large-scale signals of aerosol-cloud interactions**
29 **are frequently hampered by the considerable noise associated with meteorological co-**
30 **variability. The Iceland-Holuhraun effusive eruption in 2014 resulted in a massive aerosol**
31 **plume in an otherwise near-pristine environment and thus provided an ideal natural**
32 **experiment to quantify cloud responses to aerosol perturbations. Here we disentangle**
33 **significant signals from the noise of meteorological co-variability using a satellite-based**
34 **machine-learning approach. Our analysis shows that aerosols from the eruption**
35 **increased cloud cover by approximately 10%, and this appears to be the leading cause of**
36 **climate forcing, rather than cloud brightening as previously thought. We find that**
37 **volcanic aerosols do brighten clouds by reducing droplet size, but this has a significantly**
38 **smaller radiative impact than changes in cloud fraction. These results add substantial**
39 **observational constraints on the cooling impact of aerosols. Such constraints are critical**
40 **for improving climate models, which still inadequately represent the complex macro-**
41 **physical and micro-physical impacts of aerosol-cloud interactions.**

42

43

44

45

46 Marine low-level liquid clouds have a profound impact on the energy balance of the Earth
47 system, exerting a net cooling effect by reflecting sunlight^{1,2}. It has been previously estimated
48 that only a 6% increase of their albedo could offset the warming from a doubling of CO₂^{3,4}.
49 Aerosol-cloud interactions (ACI) are postulated to enhance albedo and prolong the lifetime of
50 liquid clouds^{5,6}, and therefore counterbalance a substantial, yet poorly constrained, portion of
51 greenhouse gas warming⁷⁻¹⁰, leading to only a small net positive overall forcing. As the Earth
52 has warmed by around 1.2 °C since pre-industrial times^{10,11}, this would imply that the Earth
53 system is highly sensitive, and therefore vulnerable, to anthropogenic climate forcing¹². Such
54 a high sensitivity would suggest a very limited remaining carbon budget if the +1.5 °C target
55 of the 21st Conference of the Parties at Paris (COP21) is to be met¹¹.

56 Despite decades of effort, ACI still contribute significantly to uncertainties in climate
57 projections^{1,7,9-11}. A primary reason for the large uncertainty in ACI is the lack of suitable large-
58 scale constraints to challenge General Circulation Models (GCMs)¹³⁻¹⁵. ACI operates through
59 processes whereby cloud droplets form on aerosol particles. For a fixed cloud liquid water path
60 (LWP), high concentrations of aerosol lead to more droplets with smaller effective radius (r_{eff} ,
61 Twomey r_{eff} effect⁵) which increases cloud albedo. Smaller cloud droplets may inhibit
62 precipitation due to weakened collision-coalescence⁶ and suppressed precipitation implies
63 clouds retain more water leading to an increased LWP (LWP adjustment), and prolong their
64 lifetime and areal extent which manifests as increased cloud fraction (CF, CF adjustment)⁶.
65 There is clear evidence of the Twomey r_{eff} effect from numerous comprehensive satellite
66 observations (e.g., ref. ^{8,15-19}), but continuous debate surrounds the LWP adjustment with
67 different magnitudes and signs reported^{8,9,15,20,21}, possibly due to confounding adjustments such
68 as effects of entrainment and droplet evaporation processes²²⁻²⁶. The CF adjustment is even
69 more difficult to constrain owing to the large-scale impacts of meteorological co-variability²⁷,
70 leading to long-standing and ongoing disputes in the scientific literature^{16,19,28-32}. Satellite

71 observational constraints of ACI tend to be limited to either small-scale observations or large-
72 scale climatological analyses³³. A typical example of a small-scale observation is “ship-tracks”,
73 manifesting as brighter lines in stratocumulus cloud decks caused by ship emissions. Such
74 small-tracks are generally able to rule out confounding meteorology^{8,19}, but with a scale far
75 below the resolution of GCMs and a short temporal signature; they are therefore not ideal
76 constraints for these models^{33,34}. Climatological analyses examine the correlations between
77 cloud properties and aerosol on a large spatiotemporal scale, but such correlations can be
78 confounded by meteorological co-variability and therefore may not confirm the causal
79 processes of ACI^{29,33,35-38}.

80 Here, we overcome these limitations by developing a meteorological reanalysis and satellite-
81 based machine-learning approach that predicts cloud properties in a near-pristine environment,
82 and compare the results with observations of clouds perturbed by the large-scale effusive
83 Icelandic eruption of Holuhraun. The machine-learning approach is enabled by an almost
84 threefold expansion of satellite data from Moderate Resolution Imaging Spectroradiometer
85 (MODIS) compared to the earlier work¹⁵, offering thus a robust training dataset. The machine-
86 learning approach allows us to quantify ACI-induced cloud responses and show an
87 unmistakable increase in cloud cover. It also allows us to infer the relative contributions to
88 ACI radiative effect from the Twomey effect, and the LWP and CF adjustments. Our results
89 improve current understanding of cloud-induced climate change, and provide robust large-
90 scale constraints for climate models.

91

92 **Volcanic aerosol perturbation**

93 The effusive volcanic eruption at Holuhraun in Iceland, emitted about 40,000 tonnes of SO₂
94 per day on average during its eruptive phase in September-October 2014 and 120,000 tonnes

95 per day at the peak of eruption^{15,39}. The sulphate aerosol formed from volcanic SO₂ interacts
96 with liquid-water clouds creating an invaluable natural experiment for testing ACI hypotheses
97 at a large-scale¹⁵. Detecting CF changes above meteorological noise requires a larger data
98 volume and was left unexplored in the previous study¹⁵, which uses the MODIS Aqua 2002-
99 2014 dataset. Here, by extending the satellite data to both MODIS Aqua and Terra and the
100 length of the analysis period to 2001-2020, we have sufficient training data to develop a robust
101 machine-learning approach for quantitatively disentangling Holuhraun eruption ACI signals
102 from the noise of meteorological co-variability (see Methods). We focus primarily on October
103 2014, because in this second eruption month the volcanic plume dispersed sufficiently across
104 the entire region of about 3000 km × 6000 km (45°N ~ 75°N; 60°W ~ 30°E, see Supplementary
105 Figure S6.2 in Malavelle et al.¹⁵). This region is an otherwise near-pristine environment and
106 encompasses the whole spectrum of liquid-dominated cloud regimes, with their frequencies of
107 occurrence being comparable to those observed globally (Extended Data Fig. 1)^{15,40}.

108 To disentangle the ACI signal from the noise of meteorological co-variability, we train a
109 machine-learning surrogate MODIS (ML-MODIS) using historical meteorology and MODIS
110 observations during 2001-2020 but excluding the year of the volcanic perturbation (2014, see
111 Methods). ML-MODIS is designed to predict cloud properties for given meteorological
112 conditions when unperturbed by volcanic aerosol. Our “leave-one-year-out” cross validation
113 (see Methods) shows that the surrogate ML-MODIS can reproduce the MODIS observations
114 of cloud droplet number concentration (N_d), r_{eff} , LWP and CF when no volcanic aerosol-
115 perturbation exists, as shown in the left column of Fig. 1. However, significant differences
116 between the ML-MODIS predictions and MODIS observations are observed in the presence of
117 the volcanic perturbation in October 2014 (right column of Fig. 1). Similar results are found
118 for September 2014 (Supplementary Discussion section S1).

119 We examine the ACI corresponding to the increase in N_d instead of aerosol optical depth,
120 because MODIS aerosol products are hampered by the overcast nature of the geographical
121 region and using N_d has several advantages as a mediating variable²⁹. We first quantify the
122 increase in N_d and then estimate the susceptibility of other cloud properties, i.e., $d\ln r_{\text{eff}}/d\ln N_d$,
123 $d\ln \text{LWP}/d\ln N_d$, and $d\ln \text{CF}/d\ln N_d$. The volcano-induced increase in N_d is observed across
124 nearly the entire region with a positive signal across the zonal means (Fig. 2a). We also observe
125 a clear shift of the N_d probability distribution towards larger values due to the volcanic
126 perturbation with an average increase of 20 cm^{-3} .

127 We perform Monte Carlo analyses (see Methods) to estimate the uncertainty of ML-MODIS
128 and to quantify the impact of ACI on relevant cloud properties. In assessing the statistical
129 uncertainties, we follow the Intergovernmental Panel on Climate Change (IPCC) uncertainty
130 guideline⁴¹ and use the 90% probabilities (that are assigned “very likely”). A validation of ML-
131 MODIS by MODIS for conditions unperturbed by Holuhraun is further achieved by these
132 results, with median and average values close to the 1:1 line (Fig. 3) and with a 90% probability
133 of the Pearson correlation coefficients (R) exceeding 0.6 for N_d , r_{eff} and CF (Extended Data
134 Fig. 2, higher than 0.5 for LWP). In contrast, the 90% probability of R being below 0.6 for all
135 cloud properties in volcano-perturbed conditions, indicates large influences of the volcanic
136 aerosol on cloud properties. We estimate a volcanic aerosol-induced increase in N_d of 28%
137 over the region (Fig. 3, showing that the ratio between ML-MODIS and MODIS is 1.27 with
138 against 0.99 without volcano), which is clearly statistically significant because the perturbation
139 lies outside the range of uncertainty of the machine-learning method. This increase is similar
140 to the ~32% increase in N_d from pre-industrial to present day according to multi-model
141 estimates¹⁴, suggesting that the results from our analysis may be a reasonable proxy for
142 anthropogenic aerosols in terms of the strength in perturbing clouds since pre-industrial times.

143

144 **Twomey effect and liquid water path adjustment**

145 We first use our machine-learning approach to examine the Twomey r_{eff} effect and LWP
146 adjustment. We observe a consistent spatial pattern of volcano-induced increase in N_d and an
147 average reduction in r_{eff} (Figs. 2a and 2b) from 15.2 μm to 13.9 μm . The spatial pattern is also
148 consistent with the climatological MODIS anomaly analysis¹⁵ (Extended Data Fig. 3), but with
149 some difference in the strength of ACI signal. This further demonstrates the viability of our
150 machine-learning approach in identifying changes in cloud created by volcanic aerosols above
151 those expected due to meteorological variability. Climatological anomalies may identify
152 regions influenced by the Holuhraun plume¹⁵ but may not be robust in quantifying ACI signals
153 arising from Holuhraun, because the ACI signal is confounded by meteorology where 2014
154 conditions are not necessarily equal to climatological average. Indeed, while Malavelle et al.¹⁵
155 developed a robust method for removing the meteorological variability in the modelled
156 response, they also cautioned that meteorological differences from the long-term mean could
157 cause some of the observed response (their Figures S6.1 and S6.2). Our machine-learning
158 approach overcomes these issues (Methods, see also Supplementary Discussion section S1 and
159 S2). We estimate an 8% decrease in r_{eff} as a response to a 28% increase in N_d on average (and
160 median) over the geographical region (Fig. 3). In line with previous studies^{8,17,31}, no significant
161 LWP response is found when examining the region as a whole (Fig. 3 and Extended Data Fig.
162 4). This may be due to the cancellation of the LWP adjustment-induced increase⁶ by
163 entrainment-induced decrease of LWP²², as suggested by Toll et al.⁸ who examined over
164 10,000 globally representative aerosol-perturbation tracks of small-scale in liquid clouds.

165

166 **Cloud fraction response**

167 So far results from our large-scale machine-learning approach agree with previous analyses: a
168 distinct and robust Twomey r_{eff} effect but a weak LWP adjustment (e.g., ref. ^{8,17,31}). We now
169 examine the adjustment of liquid phase CF, which is a macro-property of cloud and difficult to
170 examine using small-scale aerosol-induced tracks⁸. Our results of volcanic aerosol-perturbed
171 conditions show an overall increase of zonal CF at all latitudes of our domain, and a clear shift
172 of probability distribution from a median value of 0.36 to 0.39 (Fig. 2c). The CF increase
173 exhibits a spatial pattern that is consistent with the Twomey r_{eff} effect (Fig. 2b and 2c). This
174 strongly suggests that it is the aerosol perturbation that leads to increased cloud cover, since
175 the Twomey r_{eff} effect has been well documented as an ACI indicator^{8,9,15,18}.

176 We present the response of CF and other cloud properties over the geographical region using
177 the Monte Carlo method (Fig. 3). For all non-perturbed cloud properties, the validation shows
178 the median and average values on the 1:1 line. For volcano-induced changes in N_d and r_{eff} , we
179 confirm the expected increase and decrease respectively, but see little LWP response. For CF,
180 we observe a statistically significant median (and average) relative increase of 11% with the
181 signal variability range lying outside the uncertainty. We estimate $d\ln CF/d\ln N_d = 0.41$ [0.05 ~
182 1.53, 90% confidence interval], indicating a strong susceptibility of CF to aerosol-induced
183 perturbation in N_d . Rosenfeld et al.³⁰ found a similar strong susceptibility using a climatological
184 approach, but for the convective cores of southern ocean liquid clouds. This strong
185 susceptibility is also consistent with other studies (e.g. ref. ^{16,29,31,36}), although, unlike the
186 present study, their results are likely either influenced by the confounding meteorology
187 associated with the climatological correlation approach^{33,36} or limited by relatively small-scale
188 Lagrangian trajectories³³. For example, Ghan et al.¹⁴ showed that climatological correlation
189 analysis differs greatly from perturbation analysis across multiple GCMs, despite efforts to
190 classify and isolate different meteorological regimes.

191 To back up our finding of CF increase, we perform a traditional climatological anomaly
192 analysis which shows a similar spatial pattern for the CF response (Extended Data Fig. 3c).
193 Additionally, we investigate the impact of the unusually low sea-surface temperature that
194 developed to the south of the region (Extended Data Fig. 5a) owing to factors that appear to be
195 independent from the eruption⁴². While this could affect CF, it cannot be accounted for in the
196 climatological anomaly analysis using only MODIS data. Our machine-learning approach,
197 however, accounts for this variability (Extended Data Fig. 6 and Supplementary Discussion
198 section S2). We are therefore in position to better quantify a significantly weaker CF increase
199 over the corresponding region (45°N ~ 60°N, 20°W ~ 45°W; compare Fig. 2c against Extended
200 Data Fig. 3c). We also find 14% fewer cloud-free high-resolution (1-km²) MODIS pixels
201 during October 2014 compared to the long-term October mean. Again, this implies CF
202 increases in response to the volcanic aerosol. Any conceivable increase in cloud cover from
203 ice-clouds is also investigated and cannot be discerned (Extended Data Fig. 5b); this suggests
204 that any potential confounding effect from ice-cloud or transition to ice-cloud is small, and that
205 our results regarding ACI of liquid clouds are robust.

206

207 **Cloud fraction adjustment dominates radiative forcing**

208 We revisit the relative contributions to ACI-induced radiative forcing from the Twomey effect,
209 LWP and CF adjustments, see Methods section “Radiative Forcing”. In line with previous
210 studies^{8,31}, we find a weak contribution ($2 \pm 17\%$) from the LWP adjustment. However, in
211 contrast to recent studies reporting that the Twomey r_{eff} effect dominates ($> 70\%$) the ACI
212 radiative forcing^{8,19,31}; we show that, for this large-scale study across a wide range of
213 meteorological and cloud regimes, the CF adjustment ($61 \pm 23\%$) surpasses the Twomey r_{eff}
214 effect ($37 \pm 18\%$) in terms of ACI cooling (Fig. 3). This new finding may be due to the much

215 larger spatiotemporal scales of our investigation, which extends up to tens of thousands of km
216 with perturbation lasting for months. Given the large range of meteorological conditions and
217 cloud regimes included (Extended Data Fig. 1), our study appears arguably more suitable for
218 constraining large-scale climate models and ACI associated with anthropogenic emissions,
219 which themselves persist across many geographical areas and are associated with a wide variety
220 of cloud regimes.

221 Our results suggest that cooling caused by a CF increase is substantially underestimated in
222 current climate projections¹⁰. A recent multi-model assessment of the susceptibility of
223 $d\ln CF/d\ln N_d$ versus $-d\ln \tau_{\text{eff}}/d\ln N_d$ (Ghan et al.¹⁴; their Figure 1) suggests ratios of
224 approximately 1:3. Our results suggest that the CF adjustment is possibly larger than the
225 Twomey τ_{eff} effect, since the ratio of their susceptibilities is around 5:4. It is possible that GCMs
226 compensate for the lack of CF response with overly strong LWP adjustment^{8,10,15,19,34} – i.e.
227 estimate the “right” cooling but for manifestly the wrong reasons.

228 This work sheds light into certain aspects of ACI which conventionally thought to follow the
229 following route: an increase in aerosols gives rise to i) an increase in N_d leading to ii) a larger
230 number of smaller cloud droplets leading to iii) a decrease in the collision-coalescence growth
231 rate of cloud droplets, leading to iv) a reduction in precipitation leading to v) an increase in
232 LWP leading to vi) an increase in cloud lifetime leading to vii) an increase in CF. Malavelle et
233 al.¹⁵ suggested that iv) and v) do not operate as expected, while, this new study provides strong
234 evidence for vi) and vii). This conundrum needs to be addressed in further research.
235 Suggestions for how to approach this in future work includes performing large eddy model
236 simulation of the Holuhraun event to identify difference in the ACI causal chain between the
237 heavily parameterized GCMs representation and the more explicit cloud-resolving models.
238 Identifying any changes in cloud regimes (e.g., ref. ^{31,40}) might also provide further clues in

239 solving this puzzle. We maintain that because clouds are such a fundamentally important
240 component of the Earth's hydrological cycle and energy flows that the underlying reasons of
241 deficient model performance need to be urgently addressed. Our findings appear to provide
242 robust new constraints for climate models, despite the uncertainties associated with machine-
243 learning and MODIS retrievals. We acknowledge that the cold SST anomaly in October 2014
244 could potentially introduce more uncertainty in the machine-learning representation of cloud
245 conditions, but this influence appears insignificant in this study (Supplementary Discussion
246 Section S2). ACI signals are statistically significant, lying outside the uncertainty range of the
247 machine-learning approach (Fig. 3). Uncertainty in the MODIS retrievals can be decomposed
248 into systematic errors and random errors. Random errors are greatly suppressed by averaging
249 over a geographical region of thousands of kilometres⁴³, while systematic errors are largely
250 cancelled when taking differences between MODIS and ML-MODIS⁸.

251 The quantified constraints from our machine-learning study pave the way to advance our
252 current understanding of physical ACI processes, and point to new directions and challenges
253 towards future improvement of climate models. With advances in both areas, we expect that
254 our large-scale constraints on ACI will lead to reduced uncertainty in climate projections and
255 future estimates of climate sensitivity.

256

257

258

259

260

261

262 **Acknowledgments**

263 We would like to acknowledge the support of the UK Natural Environment Research Council
264 (NERC) funded ADVANCE project (NE/T006897/1) which funded JH, YC, DP, AS, DG and PF. JH, GJ
265 and FM were also part funded under funding provided by the EU's Horizon 2020 research and innovation
266 programme under the CONSTRAIN grant agreement 820829. JH, PF, GJ, AJ and FM are supported by the
267 Joint UK BEIS/Defra Met Office Hadley Centre Climate Programme (GA01101). YW would like to thank
268 the support from Mr. Philippe Sarasin and the ETH Zurich Foundation (ETH Fellowship project: 2021-HS-
269 332). DG is funded by the National Centre for Atmospheric Science (NCAS), one of the UK NERC's
270 research centres. JdL acknowledges funding from the NERC funded V-PLUS grant NE/S00436X/1. NC, LO
271 and SEP are funded by USA NASA programs. The machine-learning training is performed using the
272 "Statistics and Machine Learning Toolbox" in MATLAB (version R2019b, MathWorks Inc., Natick, MA,
273 USA). We would like to thank Ken Carslaw (University of Leeds) for co-developing and co-leading the
274 Leeds aspect of ADVANCE project, and Andy Jones (UK Met Office) for helpful discussions.

275 **Author contributions Statement**

276 YC and JH conceived the study. YW and YC designed and developed the machine-learning
277 approach used in this study with help from JH and JF. JH led the ADVANCE project funded by UK-NERC.
278 YC, FM, JG and JH performed the analysis of MODIS data with help from DG, NC, LO and SEP. NC, LO
279 and SEP performed the cloud regime analysis. YC, JH, YW, DG, UL, PF, LO, SEP, JdL, AS, DP and JF
280 contributed to the uncertainty discussion. YC and JH performed the analyses and interpreted the results with
281 inputs from all co-authors. YC and JH led the manuscript writing with specific inputs and edits from DG,
282 LO and UL. All co-authors discussed the results and commented on the manuscript.

283 **Competing Interests Statement:** The authors declare no competing interests.

284

285

286

287

288

289 **Figure Legends/Captions:**

290 **Fig. 1 | Comparison between machine-learning predictions (ML-MODIS) and MODIS**

291 **observations.** Left panels (a-d): validation against non-perturbed observations (excluding 2014) of
292 cloud properties, from top to bottom they show cloud droplet number concentration (N_d), cloud
293 droplet effective radius (r_{eff}), cloud liquid water path (LWP) and cloud fraction (CF). Right panels
294 (e-h): volcanic perturbation signals in October 2014, indicated by the difference between the machine-
295 learning predictions and the observations. October MODIS observations from Aqua (2002-2020) and
296 Terra (2001-2020) are analyzed. Colour indicates the normalized data density function with a
297 maximum value of one, with 80% of the data being contained within the black dashed area.

298 **Fig. 2 | Changes in cloud properties caused by the volcanic perturbation** estimated using
299 machine-learning predictions and MODIS observations for October 2014. The spatial distribution and
300 zonal means of the changes in N_d , r_{eff} and CF are shown in the left panels of **a-c** while right panels
301 show probability density functions (so that the areas under the curves are equivalent) for MODIS and
302 ML-MODIS.

303 **Fig. 3 | Responses of cloud properties to the volcanic aerosol-perturbation in October 2014.** The
304 aerosol-cloud interactions (ACI) signals of responses are indicated as the ratios between MODIS
305 (Aqua and Terra) observations and machine-learning predictions, i.e., Ratio = MODIS divided by
306 ML-MODIS. Uncertainties of non-perturbed baseline references are estimated using a Monte Carlo
307 method and are shown in black (see Methods, based on non-volcanic October datasets spanning 2001-
308 2020). The variability of the cloud responses to the Holuhraun volcanic aerosol perturbation are
309 shown in pink. The boxplots show 10th, 25th, median (Med.), 75th and 90th percentiles with the mean
310 value indicated by a dot. The susceptibilities of r_{eff} , LWP and CF to changes in N_d are given in a green
311 colour, median [90% confidence interval]. Area (in units of km²) weighted averaging is used to
312 calculate average cloud properties over the geographical region (Fig. 2), in order to estimate an
313 unbiased large-scale response signal. Therefore, the ratios shown here are slightly different from the
314 slopes shown in Fig. 1, in which area-weighted averaging is not applied.

315 **References:**

- 316 1 Lohmann, U. & Feichter, J. Global indirect aerosol effects: a review. *Atmos. Chem. Phys.* **5**,
 317 715-737, doi:10.5194/acp-5-715-2005 (2005).
- 318 2 L’Ecuyer, T. S., Hang, Y., Matus, A. V. & Wang, Z. Reassessing the Effect of Cloud Type on
 319 Earth’s Energy Balance in the Age of Active Spaceborne Observations. Part I: Top of
 320 Atmosphere and Surface. *Journal of Climate* **32**, 6197-6217, doi:10.1175/jcli-d-18-0753.1
 321 (2019).
- 322 3 Latham, J. *et al.* Global temperature stabilization via controlled albedo enhancement of low-
 323 level maritime clouds. *Philosophical Transactions of the Royal Society A: Mathematical,*
 324 *Physical and Engineering Sciences* **366**, 3969-3987, doi:doi:10.1098/rsta.2008.0137 (2008).
- 325 4 Chen, Y.-C., Christensen, M. W., Stephens, G. L. & Seinfeld, J. H. Satellite-based estimate of
 326 global aerosol–cloud radiative forcing by marine warm clouds. *Nature Geoscience* **7**, 643-
 327 646, doi:10.1038/ngeo2214 (2014).
- 328 5 Twomey, S. Pollution and the planetary albedo. *Atmospheric Environment* **8**, 1251-1256,
 329 doi:https://doi.org/10.1016/0004-6981(74)90004-3 (1974).
- 330 6 Albrecht, B. A. Aerosols, Cloud Microphysics, and Fractional Cloudiness. *Science* **245**, 1227-
 331 1230, doi:10.1126/science.245.4923.1227 (1989).
- 332 7 Boucher, O. *et al.* in *Climate Change 2013: The Physical Science Basis. Contribution of*
 333 *Working Group I to the Fifth Assessment Report of the Intergovernmental Panel on Climate*
 334 *Change* (eds T. F. Stocker *et al.*) 571-657 (Cambridge University Press, 2013).
- 335 8 Toll, V., Christensen, M., Quaas, J. & Bellouin, N. Weak average liquid-cloud-water response
 336 to anthropogenic aerosols. *Nature* **572**, 51-55, doi:10.1038/s41586-019-1423-9 (2019).
- 337 9 Bellouin, N. *et al.* Bounding Global Aerosol Radiative Forcing of Climate Change. *Reviews*
 338 *of Geophysics* **58**, e2019RG000660, doi:10.1029/2019rg000660 (2020).
- 339 10 IPCC. Climate Change 2021: The Physical Science Basis. Contribution of Working Group I
 340 to the Sixth Assessment Report of the Intergovernmental Panel on Climate Change [Masson-
 341 Delmotte, V., P. Zhai, A. Pirani, S.L. Connors, C. Péan, S. Berger, N. Caud, Y. Chen, L.
 342 Goldfarb, M.I. Gomis, M. Huang, K. Leitzell, E. Lonnoy, J.B.R. Matthews, T.K. Maycock, T.
 343 Waterfield, O. Yelekçi, R. Yu, and B. Zhou (eds.)]. *Cambridge University Press In Press*
 344 (2021).
- 345 11 Rogelj, J., Forster, P. M., Kriegler, E., Smith, C. J. & Séférian, R. Estimating and tracking the
 346 remaining carbon budget for stringent climate targets. *Nature* **571**, 335-342,
 347 doi:10.1038/s41586-019-1368-z (2019).
- 348 12 Andreae, M. O., Jones, C. D. & Cox, P. M. Strong present-day aerosol cooling implies a hot
 349 future. *Nature* **435**, 1187-1190 (2005).
- 350 13 Seinfeld, J. H. *et al.* Improving our fundamental understanding of the role of aerosol–cloud
 351 interactions in the climate system. *Proceedings of the National Academy of Sciences* **113**,
 352 5781-5790, doi:10.1073/pnas.1514043113 (2016).
- 353 14 Ghan, S. *et al.* Challenges in constraining anthropogenic aerosol effects on cloud radiative
 354 forcing using present-day spatiotemporal variability. *Proceedings of the National Academy of*
 355 *Sciences* **113**, 5804-5811, doi:10.1073/pnas.1514036113 (2016).
- 356 15 Malavelle, F. F. *et al.* Strong constraints on aerosol–cloud interactions from volcanic
 357 eruptions. *Nature* **546**, 485-491, doi:10.1038/nature22974 (2017).
- 358 16 Kaufman, Y. J., Koren, I., Remer, L. A., Rosenfeld, D. & Rudich, Y. The effect of smoke,
 359 dust, and pollution aerosol on shallow cloud development over the Atlantic Ocean.
 360 *Proceedings of the National Academy of Sciences of the United States of America* **102**, 11207-
 361 11212, doi:10.1073/pnas.0505191102 (2005).
- 362 17 McCoy, D. T. & Hartmann, D. L. Observations of a substantial cloud-aerosol indirect effect
 363 during the 2014–2015 Bárðarbunga-Veiðivötn fissure eruption in Iceland. *Geophysical*
 364 *Research Letters* **42**, 10,409–410,414, doi:https://doi.org/10.1002/2015GL067070 (2015).
- 365 18 Toll, V., Christensen, M., Gassó, S. & Bellouin, N. Volcano and Ship Tracks Indicate
 366 Excessive Aerosol-Induced Cloud Water Increases in a Climate Model. *Geophysical*
 367 *Research Letters* **44**, 12,492–412,500, doi:10.1002/2017gl075280 (2017).

- 368 19 Diamond, M. S., Director, H. M., Eastman, R., Possner, A. & Wood, R. Substantial Cloud
369 Brightening From Shipping in Subtropical Low Clouds. *AGU Advances* **1**, e2019AV000111,
370 doi:https://doi.org/10.1029/2019AV000111 (2020).
- 371 20 Gryspeerd, E. *et al.* Constraining the aerosol influence on cloud liquid water path. *Atmos.*
372 *Chem. Phys.* **19**, 5331-5347, doi:10.5194/acp-19-5331-2019 (2019).
- 373 21 Possner, A., Eastman, R., Bender, F. & Glassmeier, F. Deconvolution of boundary layer depth
374 and aerosol constraints on cloud water path in subtropical stratocumulus decks. *Atmos. Chem.*
375 *Phys.* **20**, 3609-3621, doi:10.5194/acp-20-3609-2020 (2020).
- 376 22 Ackerman, A. S., Kirkpatrick, M. P., Stevens, D. E. & Toon, O. B. The impact of humidity
377 above stratiform clouds on indirect aerosol climate forcing. *Nature* **432**, 1014-1017,
378 doi:10.1038/nature03174 (2004).
- 379 23 Stevens, B. & Feingold, G. Untangling aerosol effects on clouds and precipitation in a
380 buffered system. *Nature* **461**, 607-613, doi:10.1038/nature08281 (2009).
- 381 24 Lebo, Z. J. & Feingold, G. On the relationship between responses in cloud water and
382 precipitation to changes in aerosol. *Atmos. Chem. Phys.* **14**, 11817-11831, doi:10.5194/acp-
383 14-11817-2014 (2014).
- 384 25 Koren, I., Dagan, G. & Altaratz, O. From aerosol-limited to invigoration of warm convective
385 clouds. *Science* **344**, 1143-1146, doi:10.1126/science.1252595 (2014).
- 386 26 Seifert, A., Heus, T., Pincus, R. & Stevens, B. Large-eddy simulation of the transient and
387 near-equilibrium behavior of precipitating shallow convection. *Journal of Advances in*
388 *Modeling Earth Systems* **7**, 1918-1937, doi:https://doi.org/10.1002/2015MS000489 (2015).
- 389 27 Mauger, G. S. & Norris, J. R. Meteorological bias in satellite estimates of aerosol-cloud
390 relationships. *Geophysical Research Letters* **34**, doi:https://doi.org/10.1029/2007GL029952
391 (2007).
- 392 28 Kaufman, Y. J. & Koren, I. Smoke and Pollution Aerosol Effect on Cloud Cover. *Science*
393 **313**, 655-658, doi:10.1126/science.1126232 (2006).
- 394 29 Gryspeerd, E., Quaas, J. & Bellouin, N. Constraining the aerosol influence on cloud fraction.
395 *Journal of Geophysical Research: Atmospheres* **121**, 3566-3583,
396 doi:https://doi.org/10.1002/2015JD023744 (2016).
- 397 30 Rosenfeld, D. *et al.* Aerosol-driven droplet concentrations dominate coverage and water of
398 oceanic low-level clouds. *Science* **363**, eaav0566, doi:10.1126/science.aav0566 (2019).
- 399 31 Christensen, M. W., Jones, W. K. & Stier, P. Aerosols enhance cloud lifetime and brightness
400 along the stratus-to-cumulus transition. *Proceedings of the National Academy of Sciences*
401 **117**, 17591-17598, doi:10.1073/pnas.1921231117 (2020).
- 402 32 Breen, K. H., Barahona, D., Yuan, T., Bian, H. & James, S. C. Effect of volcanic emissions
403 on clouds during the 2008 and 2018 Kilauea degassing events. *Atmos. Chem. Phys.* **21**, 7749-
404 7771, doi:10.5194/acp-21-7749-2021 (2021).
- 405 33 Glassmeier, F. *et al.* Aerosol-cloud-climate cooling overestimated by ship-track data. *Science*
406 **371**, 485-489, doi:10.1126/science.abd3980 (2021).
- 407 34 Christensen, M. W. *et al.* Opportunistic experiments to constrain aerosol effective radiative
408 forcing. *Atmos. Chem. Phys.* **22**, 641-674, doi:10.5194/acp-22-641-2022 (2022).
- 409 35 Bender, F. A. M., Frey, L., McCoy, D. T., Grosvenor, D. P. & Mohrmann, J. K. Assessment
410 of aerosol–cloud–radiation correlations in satellite observations, climate models and
411 reanalysis. *Climate Dynamics* **52**, 4371-4392, doi:10.1007/s00382-018-4384-z (2019).
- 412 36 Fuchs, J., Cermak, J. & Andersen, H. Building a cloud in the southeast Atlantic:
413 understanding low-cloud controls based on satellite observations with machine learning.
414 *Atmos. Chem. Phys.* **18**, 16537-16552, doi:10.5194/acp-18-16537-2018 (2018).
- 415 37 Oreopoulos, L., Cho, N. & Lee, D. A Global Survey of Apparent Aerosol-Cloud Interaction
416 Signals. *Journal of Geophysical Research: Atmospheres* **125**, e2019JD031287,
417 doi:https://doi.org/10.1029/2019JD031287 (2020).
- 418 38 Fan, J., Wang, Y., Rosenfeld, D. & Liu, X. Review of Aerosol–Cloud Interactions:
419 Mechanisms, Significance, and Challenges. *Journal of the Atmospheric Sciences* **73**, 4221-
420 4252, doi:10.1175/jas-d-16-0037.1 (2016).
- 421 39 Gettelman, A., Schmidt, A. & Egill Kristjánsson, J. Icelandic volcanic emissions and climate.
422 *Nature Geoscience* **8**, 243-243, doi:10.1038/ngeo2376 (2015).

423 40 Oreopoulos, L., Cho, N., Lee, D. & Kato, S. Radiative effects of global MODIS cloud
424 regimes. *Journal of Geophysical Research: Atmospheres* **121**, 2299-2317,
425 doi:<https://doi.org/10.1002/2015JD024502> (2016).
426 41 IPCC. Guidance Note for Lead Authors of the IPCC Fifth Assessment Report on Consistent
427 Treatment of Uncertainties.
428 https://www.ipcc.ch/site/assets/uploads/2017/2008/AR2015_Uncertainty_Guidance_Note.pdf
429 (2010).
430 42 Grist, J. P. *et al.* Extreme air–sea interaction over the North Atlantic subpolar gyre during the
431 winter of 2013–2014 and its sub-surface legacy. *Climate Dynamics* **46**, 4027-4045,
432 doi:[10.1007/s00382-015-2819-3](https://doi.org/10.1007/s00382-015-2819-3) (2016).
433 43 Grosvenor, D. P. *et al.* Remote Sensing of Droplet Number Concentration in Warm Clouds: A
434 Review of the Current State of Knowledge and Perspectives. *Reviews of Geophysics* **56**, 409-
435 453, doi:<https://doi.org/10.1029/2017RG000593> (2018).
436

437

438

439 **Methods**

440 **MODIS observations**

441 We used the Level-3 products of MODIS Collection 6.1, i.e., MYD08 for 2002-2020 from
442 Aqua and MOD08 for 2001-2020 from Terra. The reported retrieval bias due to instrument
443 degradation in Terra-MODIS Collection 5.1 datasets¹⁵ has been rectified in Collection 6.1. An
444 inadvertent artifact in the calculations of cloud fraction (derived from cloud optical property)
445 in Collection 5.1 has also been removed in Collection 6.1⁴⁴ and both Terra-MODIS and Aqua-
446 MODIS now show consistent results^{45,46}. Cloud droplet effective radius (r_{eff}), in-cloud liquid
447 water path (LWP), cloud optical thickness and cloud phase are retrieved from observed
448 radiances using a radiative transfer model at 1-km nadir resolution in Level-2 products and
449 aggregated to the $1^\circ \times 1^\circ$ Level-3 products⁴⁶. The Level-3 Cloud Optical Property Cloud
450 Fraction product for the liquid phase (dataset name Cloud Retrieval Fraction Liquid)⁴⁶ is used
451 in the cloud fraction (CF) analysis, because this CF product can distinguish between clouds of
452 liquid and ice phase and is consistent with the other microphysical retrievals of cloud properties
453 used in this study. Note that ref. ¹⁷ used MODIS Collection 6 data, and used cloud fraction
454 derived from the cloud mask⁴⁷ multiplied by the fractional liquid cloud and found a more
455 modest increase in cloud fraction of $\sim 1.7\%$ in October. Differences between our findings and
456 those from ref. ¹⁷ in the climatological analysis likely arise from a combination of the use of
457 different CF products, the extension of the MODIS data to include data from 2015-2020, and
458 differences in the areas of investigation. Monthly-mean products are used in this study, with
459 differences being negligible when aggregating Level-3 daily products into monthly means^{15,32}.
460 An exception is liquid cloud droplet number concentration (N_d) which is derived from r_{eff} and
461 cloud optical thickness assuming adiabatic conditions^{8,20,31,48}, and because of non-linear
462 dependences, N_d is first obtained daily and then averaged to monthly means^{48,49}. Only pixels
463 with r_{eff} between $4 \mu\text{m}$ to $30 \mu\text{m}$ and cloud optical thickness between 4 to 70 are used for the

464 most reliable N_d retrievals⁴⁹. The uncertainty of the derived N_d is discussed in detail in
465 Grosvenor et al.⁴³ who estimated that the uncertainty can be largely reduced to about 50% when
466 averaged over $1^\circ \times 1^\circ$ regions. The uncertainty is expected to be even smaller in our study, since
467 we average across a geographical region of about $3000 \text{ km} \times 6000 \text{ km}$.
468 To further back up our finding of increased CF, we also analysed the frequency of cloud-free
469 conditions in arguably the most stringent MODIS product, namely pixels with retrieved aerosol
470 optical depth (AOD) at 550 nm which are used as a proxy of cloud-free pixels. This pixels are
471 most stringent because any thin or sub-grid scale cloud is screened out to prevent contamination
472 of AOD retrievals. Level-3 monthly MODIS AOD products record the number of validated 1-
473 km^2 pixels used in the Level-2 products when performing aggregation. These statistics are used
474 to calculate the relative reduction of cloud-free pixels in our region in October 2014 relative to
475 the long-term 2001-2020 October mean excluding 2014. While the number of pixels with AOD
476 retrievals do not have a one-to-one correspondence to the number of cloud-free pixels because
477 factors such as sun-glint in cloud-free pixels can reduce the number of AOD pixels, it is still a
478 good relative (rather than absolute) proxy for cloud-free pixels.

479

480 **Meteorological reanalyses**

481 Meteorological reanalyses represent the best estimate of global atmospheric conditions⁵⁰, and
482 are available from the European Centre for Medium-Range Weather Forecasts ERA5 products
483 (<https://cds.climate.copernicus.eu/>). To train the machine-learning surrogate MODIS (ML-
484 MODIS), we use the monthly averaged ERA5 reanalysis from the surface up to 550 hPa level
485 at $0.25^\circ \times 0.25^\circ$ horizontal resolution and 50 hPa vertical resolution. This vertical range covers
486 most of the low-level liquid clouds. In total, 114 meteorological parameters are re-gridded to
487 MODIS grid cells and used in the training, details of which are provided in Supplementary
488 Table S1. The ERA5 monthly reanalysis products at 11:00 and 13:00 Icelandic time (same as

489 UTC) are closest to the daytime Terra and Aqua overpass times and are paired with the
490 respective MODIS products from these satellites for the training.

491

492 **Machine-learning**

493 Previous studies that use machine-learning to investigate the statistical correlation between
494 cloud properties and aerosol (e.g., ref. ^{36,51}) can possibly be affected by confounding
495 meteorological co-variability that would prevent confirmation of the causal processes of
496 aerosol-cloud interactions (ACI)^{33,36}. Here, we use a random forest algorithm⁵² to train a ML-
497 MODIS that diagnoses cloud properties for given meteorological conditions but unperturbed
498 by volcanic aerosol. This allows comparisons of cloud properties between conditions with and
499 without volcanic aerosol-perturbation but otherwise alike, therefore quantifying cloud
500 responses only to volcanic aerosol, i.e. signals of ACI. Note that this machine-learning
501 approach is not designed to calculate the temporal evolution of cloud properties and cannot
502 predict the development of meteorological systems. The latter is obtained from the ERA5
503 reanalysis, which provides the best estimate of atmospheric state⁵⁰.

504 The random forest algorithm is chosen because of its excellent performance in dealing with
505 relatively small sample sizes and high-dimensional feature spaces and in avoiding over-
506 fitting^{52,53}. Random forest based machine-learning has been successfully applied to isolate the
507 confounding meteorological variability in air quality assessments and has been shown to
508 perform much better than multinomial regression models⁵⁴⁻⁵⁶. A regression mode forest of one
509 hundred trees is trained independently for each cloud property (N_d , r_{eff} , LWP and CF) and for
510 each month (October and September), with a minimal leaf size of seven for each tree without
511 merge leaves. Each tree samples ~60% of the input data with replacement for the training data
512 and the remaining data is used as out-of-bag observations. With larger forests, we find a
513 negligible reduction in out-of-bag mean squared error and a negligible increase in out-of-bag

514 coefficient of determination (a more informative estimate of performance than mean squared
515 error⁵⁷) of up to 0.87 for CF prediction. This indicates a good stability and avoidance of over-
516 fitting⁵⁸. The number of randomly selected predictors is 38 (one third of the total number of
517 features) and the interactive-curvature method is used to select split predictors. The ERA5
518 meteorological reanalysis is independent of the MODIS datasets, which are not assimilated in
519 the reanalysis⁵⁰, and provides the explanatory variables in the ML-MODIS training. The
520 dependent variables are the corresponding cloud properties observed by MODIS with no
521 volcanic eruption. The successful training of ML-MODIS is enabled by the large MODIS
522 dataset from continuous observations over the past 20 years on two satellite platforms. We
523 employ the “out-of-bag permuted predictor delta error” method^{52,59} to measure the importance
524 of each explanatory feature in predicting cloud properties. The results for CF shown in
525 Extended Data Fig. 6.

526 The performance of ML-MODIS as a surrogate of the MODIS observations under conditions
527 without the volcanic perturbation is evaluated using “leave-one-year-out” cross validation⁶⁰ for
528 each cloud property, as shown in the left panels of Fig. 1 and Extended Data Fig. 7. This
529 involves training ML-MODIS using randomly selected sets of 18 years of ERA5-MODIS
530 dataset pairs and then evaluating ML-MODIS against the remaining 19th year of MODIS
531 observations. This evaluation is carried out for each non-eruption year during 2001-2020. The
532 uncertainty of ML-MODIS is further estimated using a Monte Carlo method, and the variability
533 of the reference baselines are shown as black boxplots in Fig. 3 and Extended Data Fig. 8a. For
534 the Monte Carlo uncertainty estimate, we randomly perform “leave-one-year-out” validation
535 500 times for each cloud property, by excluding both Terra and Aqua datasets of the randomly
536 selected year over the entire region from machine-learning training but use them for validation.
537 A test for N_d using the validation of a 700-member Monte Carlo ensemble showed negligible
538 differences. The ratios of cloud properties between the ML-MODIS prediction (without

539 volcano-perturbation) and MODIS observations in 2014 (with volcano-perturbation) are in
 540 pink in Fig. 3 for October and in Extended Data Fig. 8a for September, with the pink boxplots
 541 showing the variability of all decision-trees within the random forest Monte Carlo ensembles,
 542 i.e., the variability of the ACI signals.

543

544 Radiative forcing

545 We estimate the relative contributions from the Twomey r_{eff} , LWP adjustment, and CF
 546 adjustment to ACI-induced radiative forcing using the susceptibilities of r_{eff} , LWP and CF to
 547 N_d perturbations. The radiative forcing arising from cloud albedo brightening can be described
 548 as Eq. (1) at a constant CF^{8,9,61}, and the forcing arising from CF enhancement can be described
 549 as Eq. (2) at a constant cloud albedo α_{cld} .

$$\left. \frac{dSW_{\text{TOA}}}{d \ln AOD} \right|_{CF} = -SW_{\text{down}} \times CF \times \alpha_{\text{cld}} \times (1 - \alpha_{\text{cld}}) \times \frac{d \ln N_d}{d \ln AOD} \times \left(\frac{1}{3} + \frac{5}{6} \frac{d \ln LWP}{d \ln N_d} \right) \quad (1)$$

550

$$\left. \frac{dSW_{\text{TOA}}}{d \ln AOD} \right|_{\text{albedo}} = -SW_{\text{down}} \times (\alpha_{\text{cld}} - \alpha_{\text{cs}}) \times \frac{dCF}{d \ln AOD} = -SW_{\text{down}} \times (\alpha_{\text{cld}} - \alpha_{\text{cs}}) \times CF \times \frac{d \ln CF}{d \ln N_d} \times \frac{d \ln N_d}{d \ln AOD} \quad (2)$$

551 where dSW_{TOA} is the short-wave radiative forcing at the top of atmosphere, SW_{down} is the
 552 incoming short-wave solar radiation at the top of the atmosphere, α_{cld} is the average broadband
 553 short-wave cloud albedo with a global mean of 0.38 for liquid clouds⁹, and α_{cs} is clear-sky
 554 broadband ocean surface albedo which is about 0.07 for representative of global average (solar
 555 zenith angle of 60 degrees)⁶². The total ACI-induced short-wave radiative forcing is the sum
 556 of Eq. (1) and Eq. (2), as shown in Eq. (3).

$$\begin{aligned} \frac{dSW_{\text{TOA}}}{d \ln AOD} &= \left. \frac{dSW_{\text{TOA}}}{d \ln AOD} \right|_{\text{albedo}} + \left. \frac{dSW_{\text{TOA}}}{d \ln AOD} \right|_{CF} \\ &= -SW_{\text{down}} \times CF \times \frac{d \ln N_d}{d \ln AOD} \times \left[\frac{1}{3} \alpha_{\text{cld}} (1 - \alpha_{\text{cld}}) + \alpha_{\text{cld}} (1 - \alpha_{\text{cld}}) \times \frac{5}{6} \frac{d \ln LWP}{d \ln N_d} + (\alpha_{\text{cld}} - \alpha_{\text{cs}}) \frac{d \ln CF}{d \ln N_d} \right] \end{aligned} \quad (3)$$

557 The radiative forcing contributions from the Twomey r_{eff} effect, LWP adjustment and CF
558 adjustment are described as the three terms in the square bracket from left to right, respectively.

559

560 **Data availability:** The MODIS cloud and aerosol products from Aqua (MYD08_L3) and Terra
561 (MOD08_L3) used in this study are available from the Atmosphere Archive and Distribution System
562 Distributed Active Archive Center of National Aeronautics and Space Administration (LAADS-DAAC,
563 NASA), <https://ladsweb.modaps.eosdis.nasa.gov>. ERA5 datasets are available from the European Centre for
564 Medium-range Weather Forecast (ECMWF) archive, <https://cds.climate.copernicus.eu>. The full datasets
565 shown in the figures are provided in source data files.

566 **Code availability:** Code is available from the corresponding author on reasonable request.

567

568 **References for Methods and Supplementary Information:**

- 569 44 Platnick, A. S. *et al.* MODIS Cloud Optical Properties: User Guide for the Collection 6/6.1
570 Level-2 MOD06/MYD06 Product and Associated Level-3 Datasets. [https://atmosphere-](https://atmosphere-imager.gsfc.nasa.gov/sites/default/files/ModAtmo/MODISCloudOpticalPropertyUserGuideFinal_v1.1_1_1.pdf)
571 *imager.gsfc.nasa.gov/sites/default/files/ModAtmo/MODISCloudOpticalPropertyUserGuideFi-*
572 *nal_v1.1_1_1.pdf* (2018).
- 573 45 Platnick, S. *et al.* The MODIS Cloud Optical and Microphysical Products: Collection 6
574 Updates and Examples From Terra and Aqua. *IEEE Transactions on Geoscience and Remote*
575 *Sensing* **55**, 502-525, doi:10.1109/TGRS.2016.2610522 (2017).
- 576 46 Hubanks, P., Platnick, A. S., King, M. & Ridgway, B. MODIS Atmosphere L3 Gridded
577 Product Algorithm Theoretical Basis Document (ATBD) & Users Guide. *available from:*
578 *https://icdc.cen.uni-*
579 *hamburg.de/fileadmin/user_upload/icdc_Dokumente/MODIS/MODIS_Collection6_Atmosphe-*
580 *reL3_GriddedProduct_ATBDandUsersGuide_v4.1_Sep22_2015.pdf* (2019).
- 581 47 Maddux, B. C., Ackerman, S. A. & Platnick, S. Viewing Geometry Dependencies in MODIS
582 Cloud Products. *Journal of Atmospheric and Oceanic Technology* **27**, 1519-1528,
583 doi:10.1175/2010jtecha1432.1 (2010).
- 584 48 Quaas, J., Boucher, O., Bellouin, N. & Kinne, S. Satellite-based estimate of the direct and
585 indirect aerosol climate forcing. *Journal of Geophysical Research: Atmospheres* **113**,
586 doi:<https://doi.org/10.1029/2007JD008962> (2008).
- 587 49 Quaas, J., Boucher, O. & Lohmann, U. Constraining the total aerosol indirect effect in the
588 LMDZ and ECHAM4 GCMs using MODIS satellite data. *Atmos. Chem. Phys.* **6**, 947-955,
589 doi:10.5194/acp-6-947-2006 (2006).
- 590 50 Hersbach, H. *et al.* The ERA5 global reanalysis. *Quarterly Journal of the Royal*
591 *Meteorological Society* **146**, 1999-2049, doi:<https://doi.org/10.1002/qj.3803> (2020).
- 592 51 Andersen, H., Cermak, J., Fuchs, J., Knutti, R. & Lohmann, U. Understanding the drivers of
593 marine liquid-water cloud occurrence and properties with global observations using neural
594 networks. *Atmos. Chem. Phys.* **17**, 9535-9546, doi:10.5194/acp-17-9535-2017 (2017).
- 595 52 Breiman, L. Random Forests. *Machine Learning* **45**, 5-32, doi:10.1023/A:1010933404324
596 (2001).
- 597 53 Biau, G. & Scornet, E. A random forest guided tour. *TEST* **25**, 197-227, doi:10.1007/s11749-
598 016-0481-7 (2016).

599 54 Grange, S. K., Carslaw, D. C., Lewis, A. C., Boleti, E. & Hueglin, C. Random forest
600 meteorological normalisation models for Swiss PM10 trend analysis. *Atmos. Chem. Phys.* **18**,
601 6223-6239, doi:10.5194/acp-18-6223-2018 (2018).

602 55 Shi, Z. *et al.* Abrupt but smaller than expected changes in surface air quality attributable to
603 COVID-19 lockdowns. *Science Advances* **7**, eabd6696, doi:10.1126/sciadv.abd6696 (2021).

604 56 Yang, J. *et al.* From COVID-19 to future electrification: Assessing traffic impacts on air
605 quality by a machine-learning model. *Proceedings of the National Academy of Sciences* **118**,
606 e2102705118, doi:10.1073/pnas.2102705118 (2021).

607 57 Chicco, D., Warrens, M. J. & Jurman, G. The coefficient of determination R-squared is more
608 informative than SMAPE, MAE, MAPE, MSE and RMSE in regression analysis evaluation.
609 *PeerJ Computer Science* **7**, e623, doi:10.7717/peerj-cs.623 (2021).

610 58 Cutler, A., Cutler, D. R. & Stevens, J. R. Random Forests. In: Zhang C., Ma Y. (eds)
611 Ensemble Machine Learning. . Springer, Boston, MA. , doi:https://doi.org/10.1007/978-1-
612 4419-9326-7_5 (2012).

613 59 Bonte, S., Goethals, I. & Holen, R. V. in *2017 IEEE Nuclear Science Symposium and Medical
614 Imaging Conference (NSS/MIC)*. 1-3.

615 60 Bastos, L. S. & O'Hagan, A. Diagnostics for Gaussian Process Emulators. *Technometrics* **51**,
616 425-438, doi:10.1198/TECH.2009.08019 (2009).

617 61 Ackerman, A. S. *et al.* Effects of Aerosols on Cloud Albedo: Evaluation of Twomey's
618 Parameterization of Cloud Susceptibility Using Measurements of Ship Tracks. *Journal of the
619 Atmospheric Sciences* **57**, 2684-2695, doi:10.1175/1520-
620 0469(2000)057<2684:eoaoa>2.0.co;2 (2000).

621 62 Jin, Z., Charlock, T. P., Smith Jr., W. L. & Rutledge, K. A parameterization of ocean surface
622 albedo. *Geophysical Research Letters* **31**, doi:https://doi.org/10.1029/2004GL021180 (2004).

623 63 Twigg, M. M. *et al.* Impacts of the 2014–2015 Holuhraun eruption on the UK atmosphere.
624 *Atmos. Chem. Phys.* **16**, 11415-11431, doi:10.5194/acp-16-11415-2016 (2016).

625 64 Myers, T. A. & Norris, J. R. On the Relationships between Subtropical Clouds and
626 Meteorology in Observations and CMIP3 and CMIP5 Models. *Journal of Climate* **28**, 2945-
627 2967, doi:10.1175/jcli-d-14-00475.1 (2015).

628 65 Höjgård-Olsen, E. *Observations of the tropical atmospheric water cycle and its variations
629 with sea surface temperature using a constellation of satellites Observations du cycle de l'eau
630 atmosphérique tropicale et de ses variations avec la température de surface de la mer, à
631 l'aide d'une constellation de satellites*, Université Paris-Saclay, (2020).

632 66 Costa, A. A., Cotton, W. R., Walko, R. L., Pielke, R. A. & Jiang, H. SST Sensitivities in
633 Multiday TOGA COARE Cloud-Resolving Simulations. *Journal of the Atmospheric Sciences*
634 **58**, 253-268, doi:10.1175/1520-0469(2001)058<0253:Ssimtc>2.0.Co;2 (2001).

635 67 Sandu, I., Stevens, B. & Pincus, R. On the transitions in marine boundary layer cloudiness.
636 *Atmos. Chem. Phys.* **10**, 2377-2391, doi:10.5194/acp-10-2377-2010 (2010).

637

638

639

640

641

642

643

644

645

646

647
648

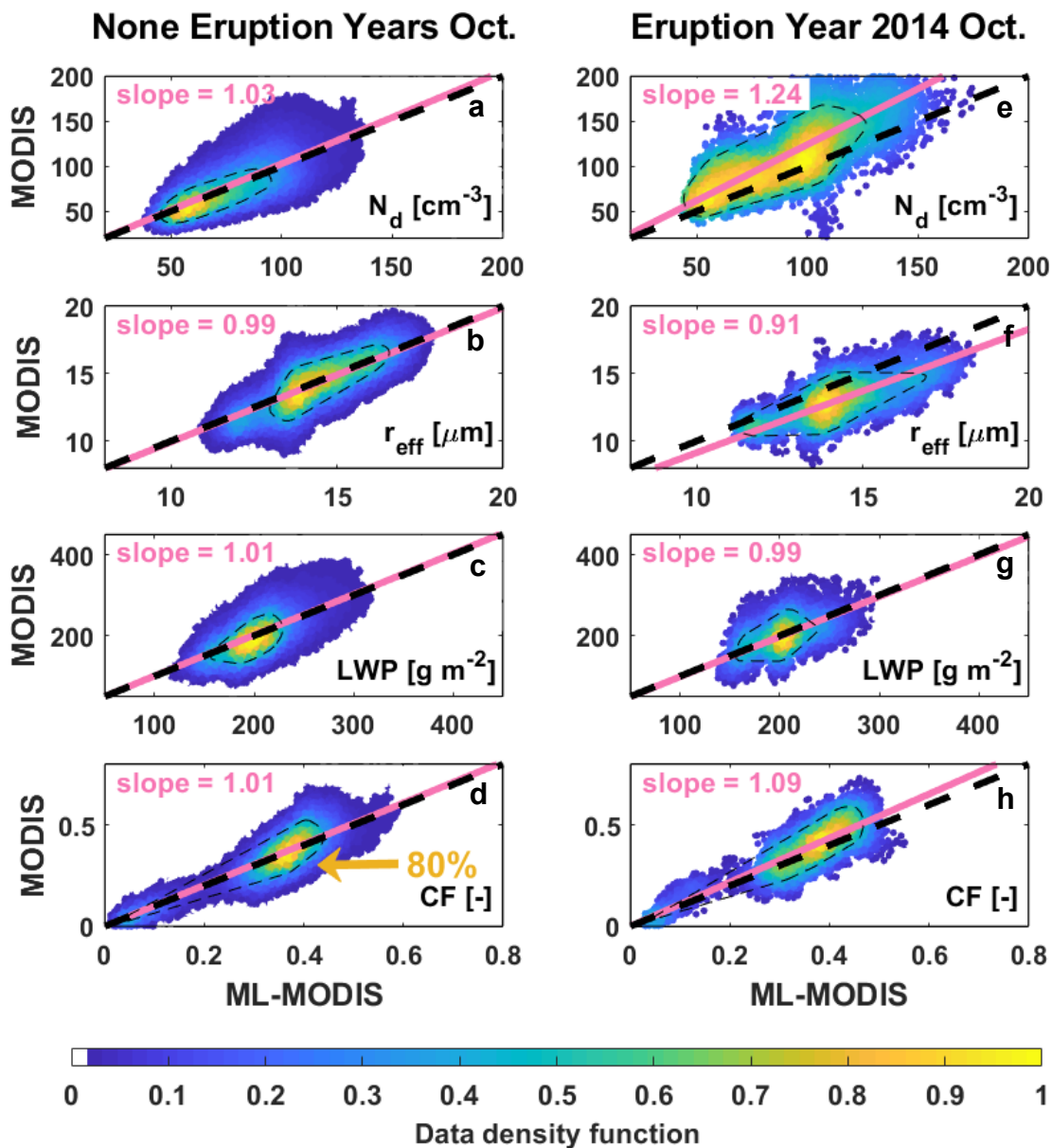


Fig. 1 | Comparison between machine-learning predictions (ML-MODIS) and MODIS observations. Left panels (a-d): validation against non-perturbed observations (excluding 2014) of cloud properties, from top to bottom they show cloud droplet number concentration (N_d), cloud droplet effective radius (r_{eff}), cloud liquid water path (LWP) and cloud fraction (CF). Right panels (e-h): volcanic perturbation signals in October 2014, indicated by the difference between the machine-learning predictions and the observations. October MODIS observations from Aqua (2002-2020) and Terra (2001-2020) are analyzed. Colour indicates the normalized data density function with a maximum value of one, with 80% of the data being contained within the black dashed area.

649
650
651
652

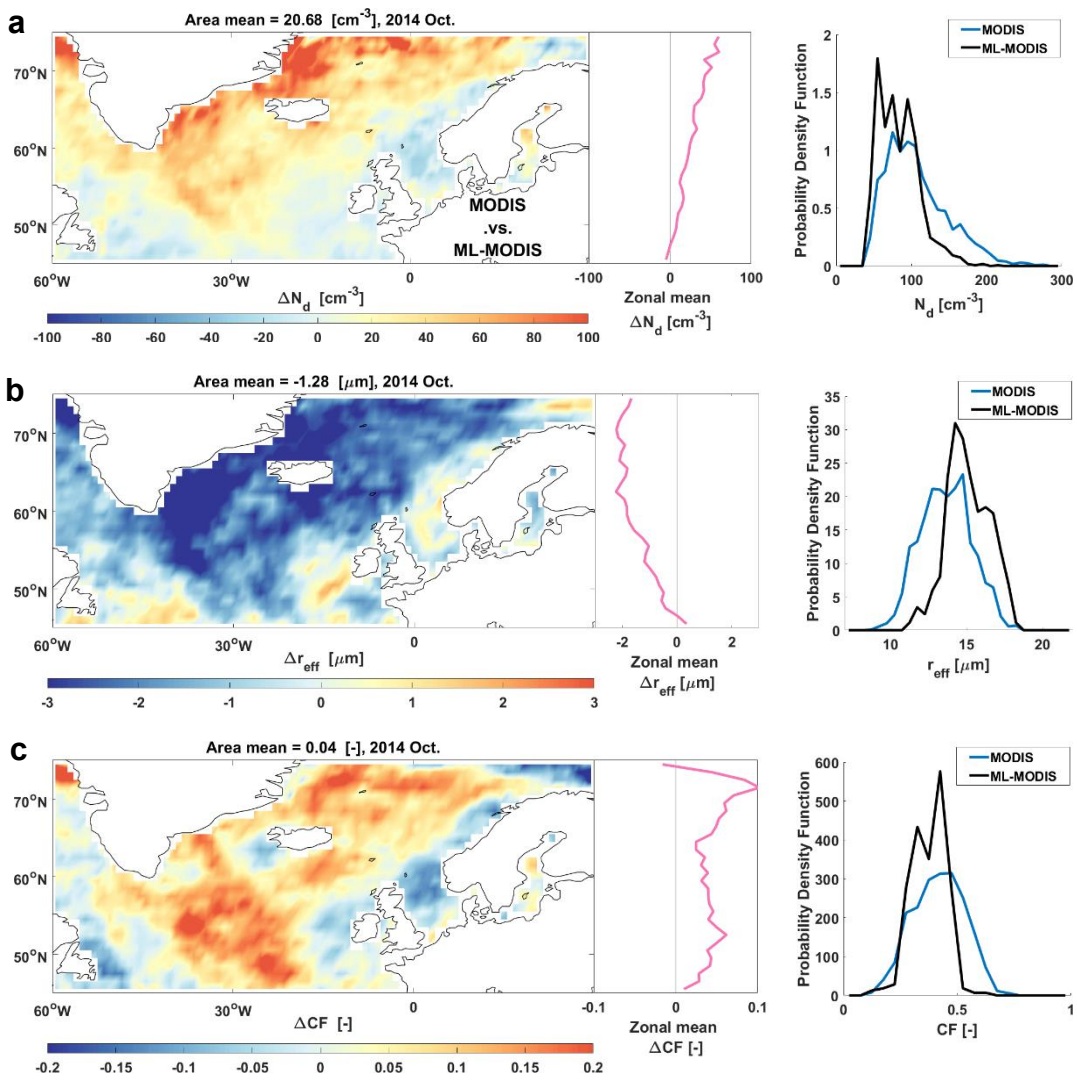


Fig. 2 | Changes in cloud properties caused by the volcanic perturbation estimated using machine-learning predictions and MODIS observations for October 2014. The spatial distribution and zonal means of the changes in N_d , r_{eff} and CF are shown in the left panels of **a-c** while right panels show probability density functions (so that the areas under the curves are equivalent) for MODIS and ML-MODIS.

654

655

656

657

658

659

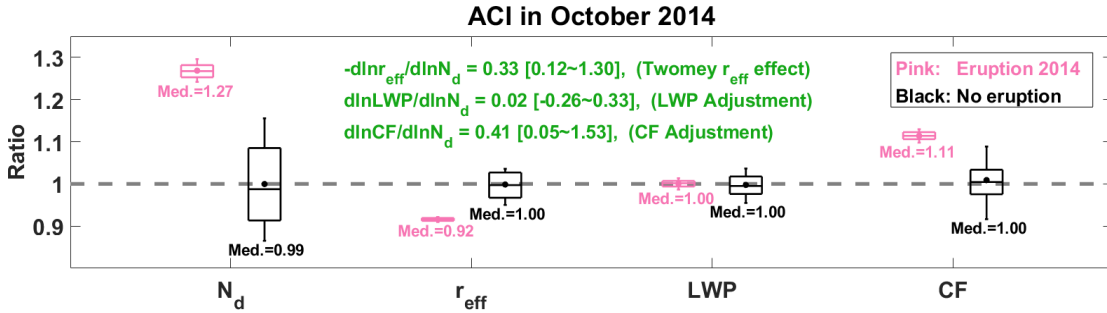


Fig. 3 | Responses of cloud properties to the volcanic aerosol-perturbation in October 2014. The aerosol-cloud interactions (ACI) signals of responses are indicated as the ratios between MODIS (Aqua and Terra) observations and machine-learning predictions, i.e., Ratio = MODIS divided by ML-MODIS. Uncertainties of non-perturbed baseline references are estimated using a Monte Carlo method and are shown in black (see Methods, based on non-volcanic October datasets spanning 2001-2020). The variability of the cloud responses to the Holuhraun volcanic aerosol perturbation are shown in pink. The boxplots show 10th, 25th, median (Med.), 75th and 90th percentiles with the mean value indicated by a dot. The susceptibilities of r_{eff} , LWP and CF to changes in N_d are given in a green colour, median [90% confidence interval]. Area (in units of km²) weighted averaging is used to calculate average cloud properties over the geographical region (Fig. 2), in order to estimate an unbiased large-scale response signal. Therefore, the ratios shown here are slightly different from the slopes shown in Fig. 1, in which area-weighted averaging is not applied.

660
 661
 662
 663
 664
 665
 666
 667
 668
 669
 670
 671
 672
 673
 674
 675
 676
 677
 678

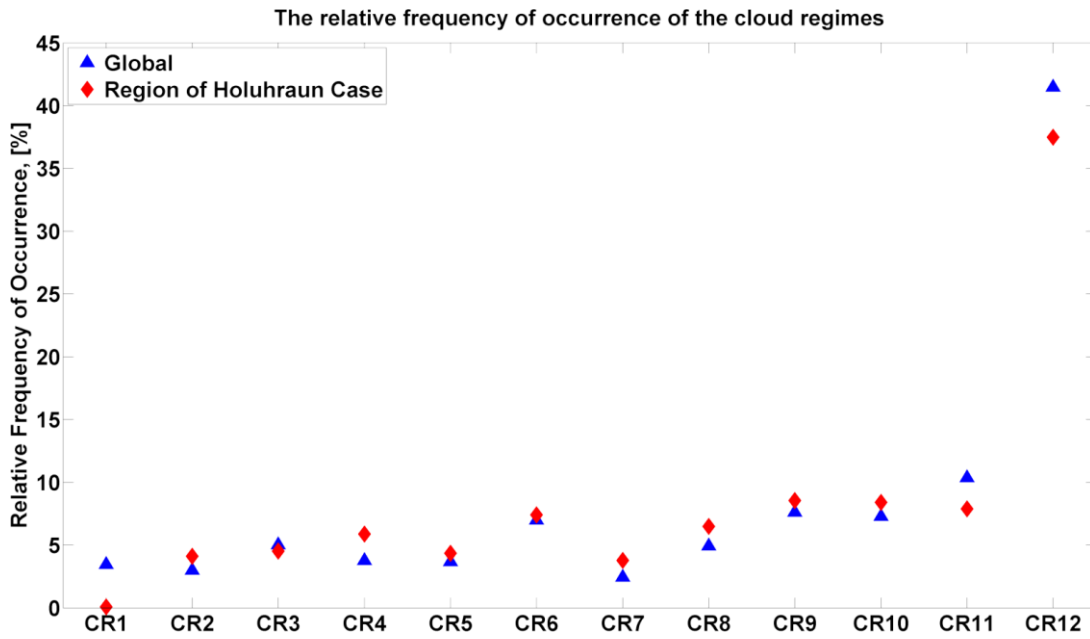
679

680 Extended Data Figures.

681

682

683

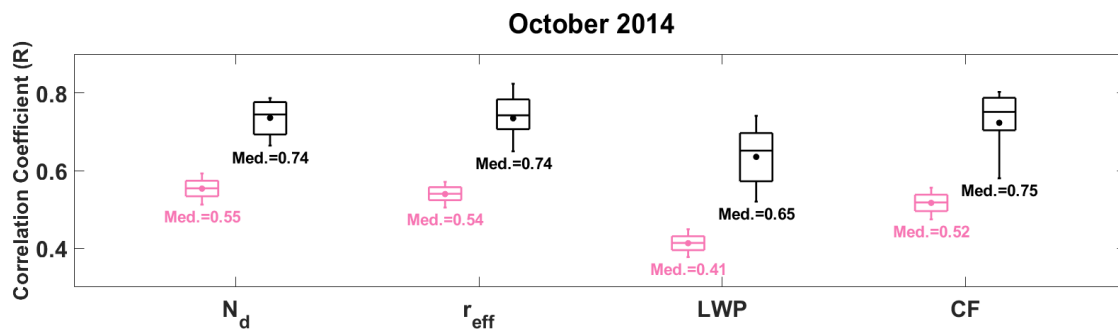


Extended Data Fig. 1 | Relative frequency of occurrence (RFO) of cloud regimes. The RFO values of the region studied here in September-October 2014 are given in red diamonds, data sourced from Malavelle et al.¹⁵. The RFO values during 2002-2014 globally are given in blue triangles, data sourced from Oreopoulos et al.⁴⁰. CR6-CR11 are liquid-dominated cloud regimes, and the others are ice-dominated cloud regimes. The details of each cloud regime are given in the above references accordingly.

684

685

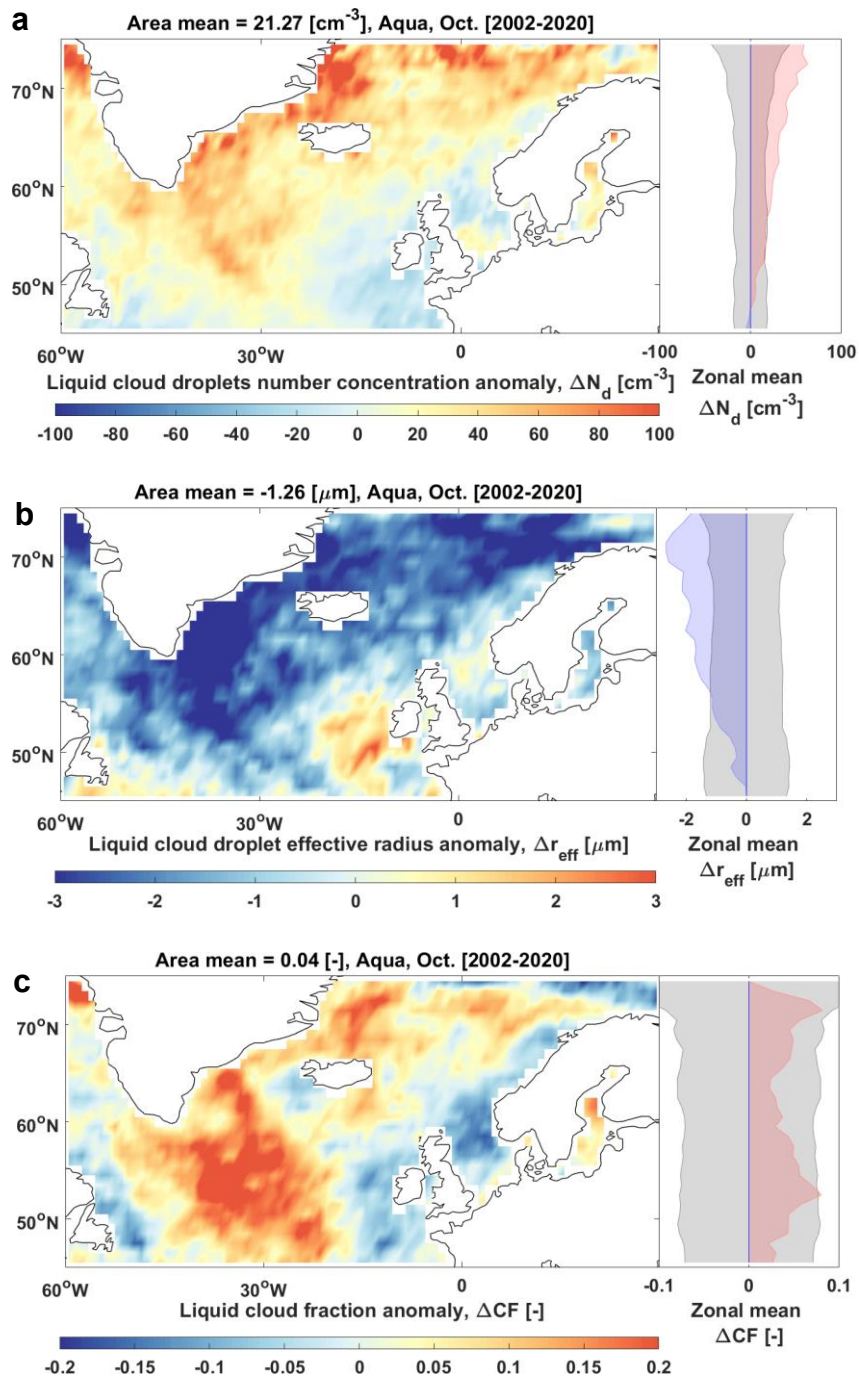
686



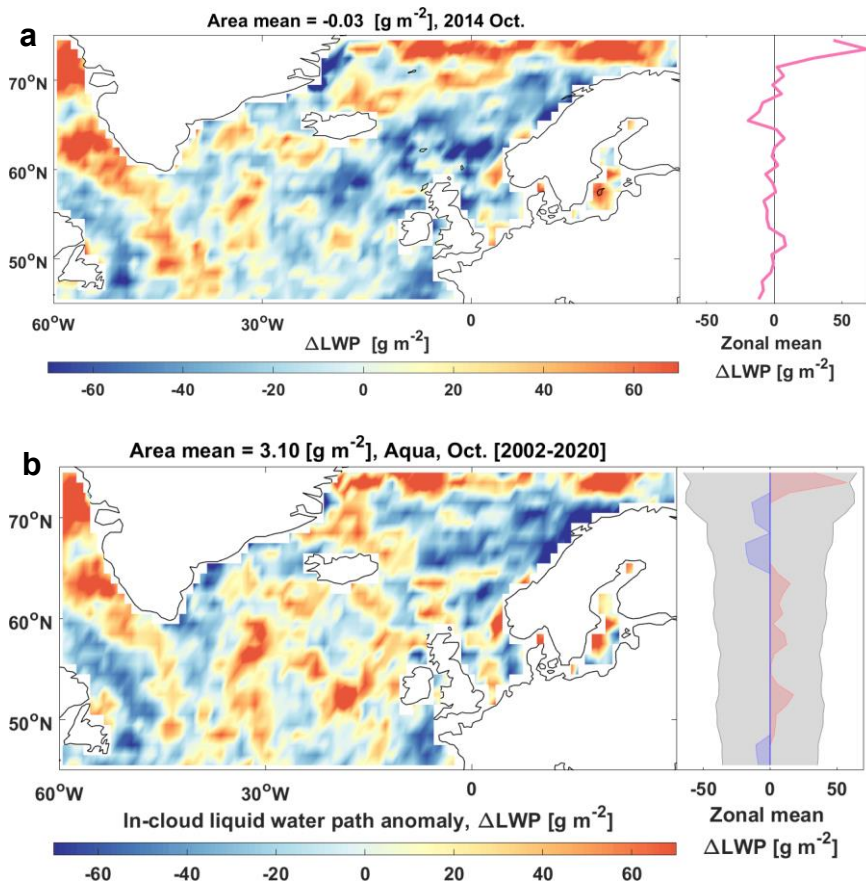
Extended Data Fig. 2 | Correlation coefficient between machine-learning predictions and MODIS observations of cloud properties, including liquid cloud droplet number concentration (N_d), liquid droplet effective radius (r_{eff}), liquid water path (LWP) and liquid cloud fraction (CF). The Monte Carlo results of ML-MODIS validation against MODIS observations without volcanic aerosol-perturbation are given in black. The variations of comparisons with volcanic aerosol-perturbation in October 2014 are given in pink. The boxplot shows 10th, 25th, median (Med.), 75th and 90th percentiles with the mean value indicated by a dot.

687

688

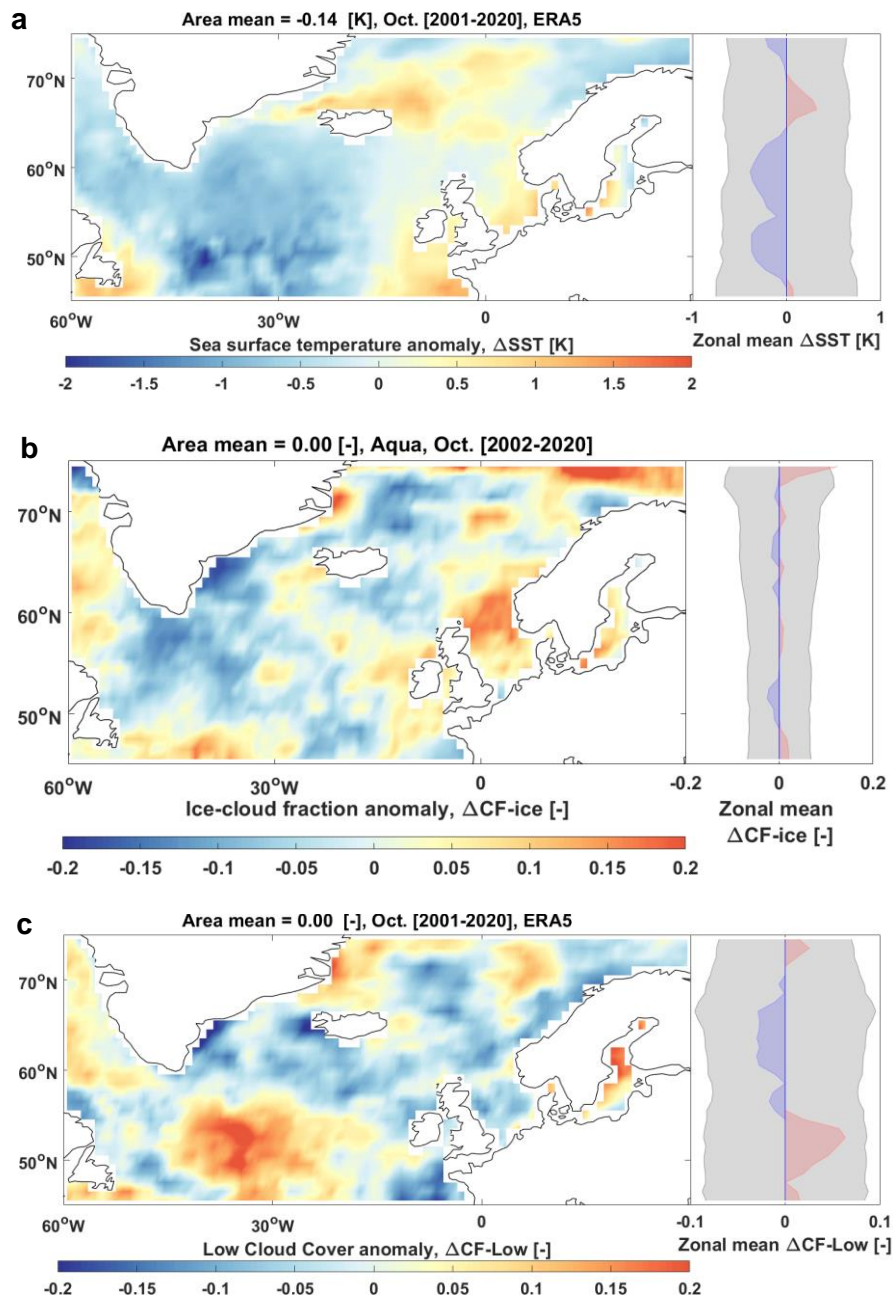


Extended Data Fig. 3 | Anomalies in MODIS-Aqua cloud properties for October 2014. The spatial distributions and zonal means of anomalies in N_d , r_{eff} and CF are shown in the panels a-c. Anomalies correspond to the deviation from the 2002-2020 climatology (excluding the 2014 eruption year). The positive anomalies are shown in red and negative ones in blue. The standard deviation is shown by the grey shading.



Extended Data Fig. 4 | Change (a) and anomaly (b) in liquid water path (LWP). a) Similar to Fig. 2, changes are detected using machine-learning; b) similar to Extended Data Fig. 3, anomaly corresponds to the deviation from 2002-2020 climatology.

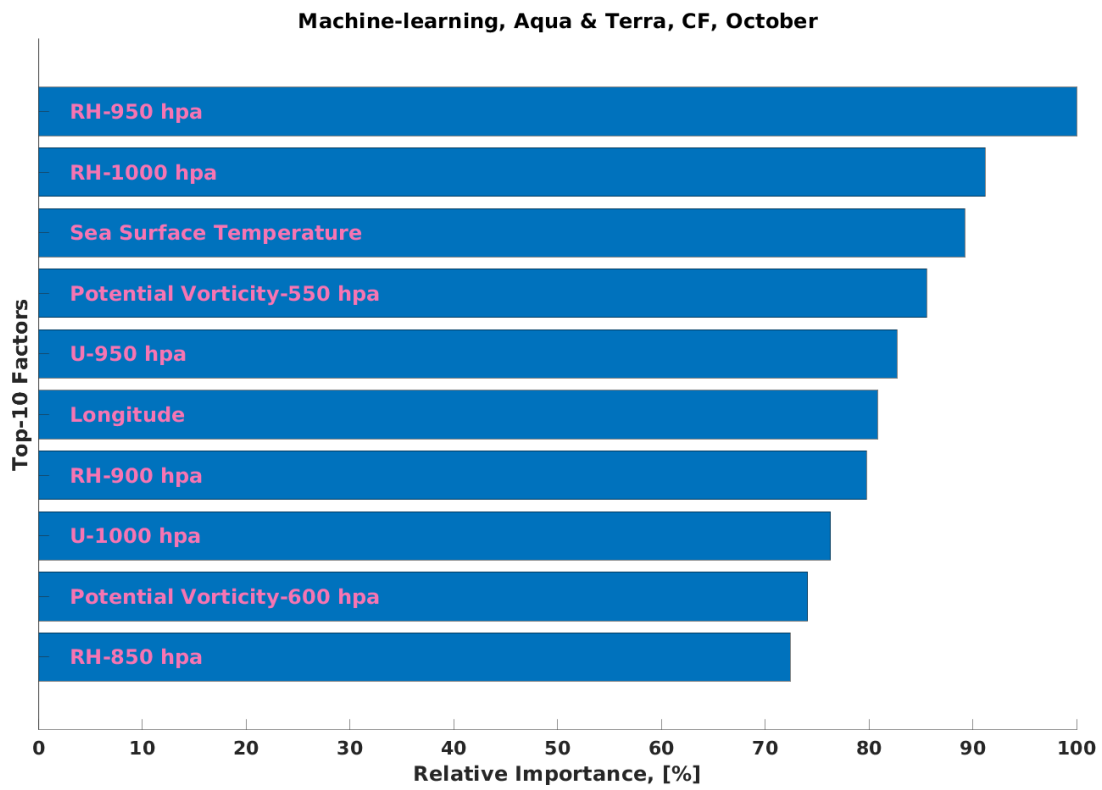
692
 693
 694
 695
 696
 697
 698
 699
 700
 701
 702
 703



Extended Data Fig. 5 | Similar to Extended Data Fig. 3, but show anomaly in sea-surface temperature (a), anomaly in ice-cloud fraction in October 2014 (b), and climatological anomaly of low-level cloud cover in October 2014 using ERA5 reanalysis (c).

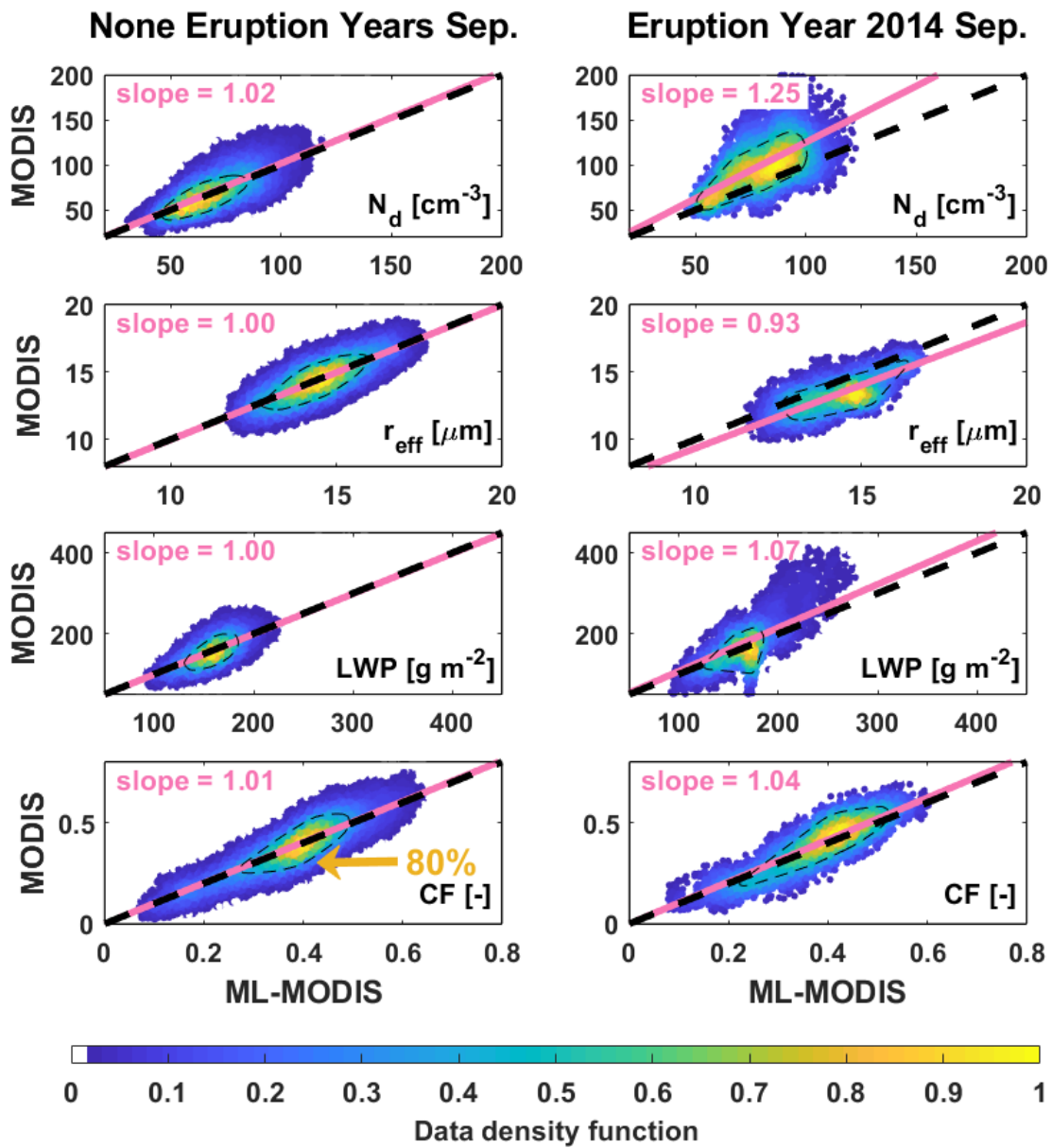
704
705
706
707
708
709
710

711
712
713
714
715
716



Extended Data Fig. 6 | The top-10 most important features for machine-learning to predict unperturbed liquid cloud fraction in October. The feature importance is normalized with the maximum as 100%. The value of these features in 2014 are entirely within the variation range of machine-learning training dataset, see Extended Data Fig. 10.

717
718
719
720



Extended Data Fig. 7 | Similar to Fig. 1, but show results in September 2014.

722

723

724

725

726

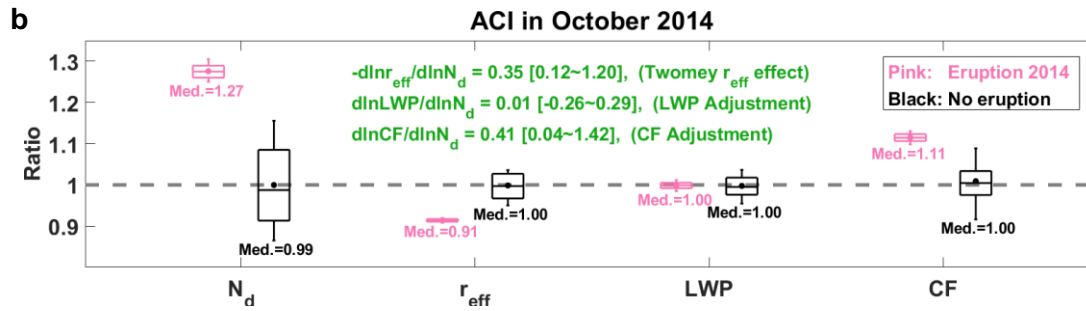
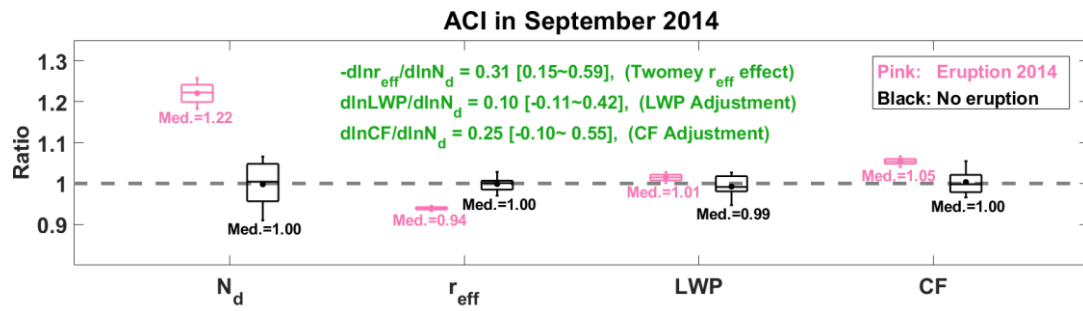
727

728

729

730

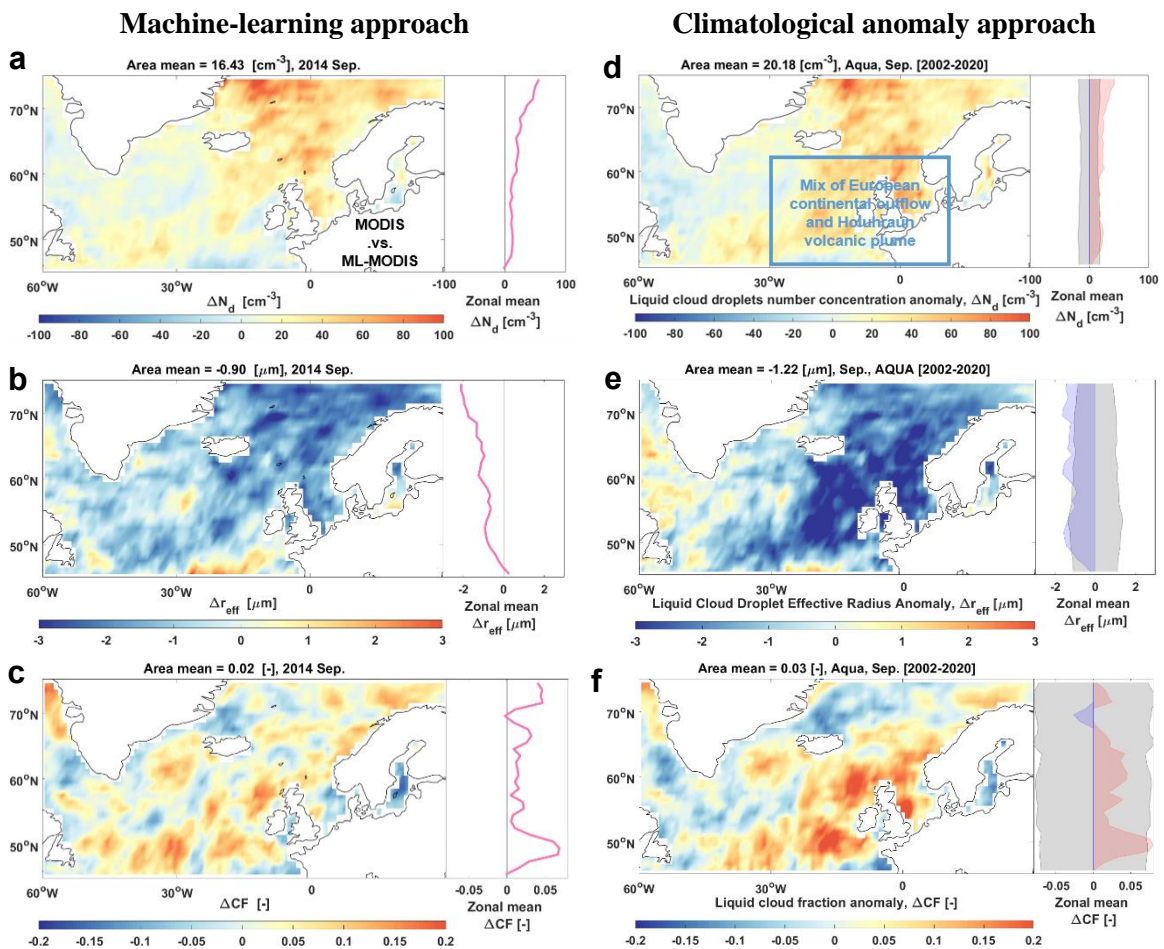
a



Extended Data Fig. 8 | Similar to Fig. 3. Panel a shows results in September 2014. **Panel b** shows results in October 2014 but excluding the regions where the cold anomalous SSTs were outside the variation range at the same location.

731

732



Extended Data Fig. 9 | Cloud responses to Holuhraun volcanic aerosol in September 2014. Left panels a-c (similar to Fig. 2 but for September 2014) show cloud responses to volcanic aerosol using machine-learning (ML) approach. Right panels d-f (similar to Extended Data Fig. 3 but for September 2014) show anomalies in cloud properties.

734

735

736

737

738

739

740

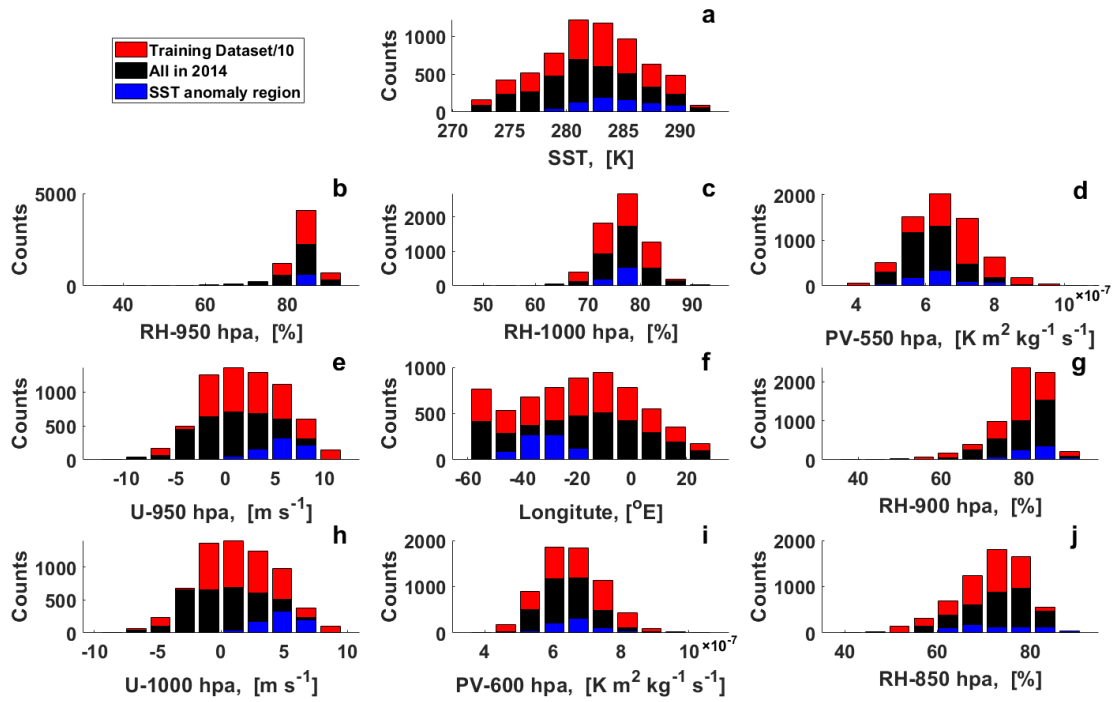
741

742

743

744

745



Extended Data Fig. 10 | Probability distribution of the top-10 most important features, as shown in Extended Data Fig. 6. Red bars indicate the counts (scaled by 0.1 to fit the display range) of the training data in each bin, which covers the entire variability range of black and blue bars; black bars indicate the data counts from the entire studied region in October 2014; and blue bars indicate the counts from the SST anomaly region only. Note that the counts per longitude are different, because we only consider data over the oceans.

746

747

748